PHYSICAL REVIEW A **100**, 053411 (2019)

Semiclassical two-step model with quantum input: Quantum-classical approach to strong-field ionization

N. I. Shvetsov-Shilovski[*] and M. Lein
Institut für Theoretische Physik, Leibniz Universität Hannover, D-30167 Hannover, Germany

(Received 2 July 2019; published 18 November 2019)

We present a mixed quantum-classical approach to strong-field ionization—a semiclassical two-step model with quantum input. In this model the initial conditions for classical trajectories that simulate an electron wave packet after ionization are determined by the exact quantum dynamics. As a result, the model allows to overcome deficiencies of standard semiclassical approaches in describing the ionization step. The comparison with the exact numerical solution of the time-dependent Schrödinger equation shows that for ionization of a one-dimensional atom the model yields quantitative agreement with the quantum result. This applies both to the width of the photoelectron momentum distribution and to the interference structure.

DOI: 10.1103/PhysRevA.100.053411

I. INTRODUCTION

Strong-field physics is a fascinating field of research resulting from remarkable progress in laser technologies during the last three decades. The interaction of strong laser radiation with atoms and molecules leads to many highly nonlinear phenomena, including above-threshold ionization (ATI) along with the formation of the plateau in the energy spectrum of the photoelectrons (high-order ATI), generation of high-order harmonics of the incident field (HHG), and nonsequential double ionization (NSDI) (see, e.g., Refs. [1–5] for reviews). The main theoretical approaches used to study all these phenomena are based on the strong-field approximation (SFA) [6–8], direct numerical solution of the time-dependent Schrödinger equation (TDSE) (see, e.g, Refs. [9–14] and references therein), and the semiclassical models.

The semiclassical models apply classical mechanics to describe the motion of an electron after it has been released from an atom or molecule by a strong laser field. The most widely known examples of the semiclassical approaches are the two-step [15–17] and the three-step [18,19] models. The two-step model corresponds to the following picture of the ionization process. In the first step an electron is promoted into the continuum, typically by tunneling ionization [20–22]. In the second step the electron moves in the laser field towards a detector along a classical trajectory. In addition to these two steps, the three-step model involves the interaction of the returning electron with the parent ion. Accounting for this interaction allows the three-step model to qualitatively describe high-order ATI, HHG, and NSDI.

The semiclassical approaches have important advantages. First, the trajectory-based models, including those that take into account both the laser field and the ionic potential, are often computationally simpler than the numerical solution of the TDSE. What is even more important, the analysis of the classical trajectories helps to understand the physical picture of the strong-field phenomenon under study.

In order to calculate the classical trajectory, it is necessary to specify the corresponding initial conditions, i.e., the starting point and the initial velocity of the electron. To obtain the former, i.e., the tunnel exit point, the separation of the tunneling problem for the Coulomb potential in parabolic coordinates can be used (see, e.g., Ref. [20]). In trajectory-based models it is often assumed that the electron starts with zero initial velocity along the laser field. Simultaneously, it can have a nonzero initial velocity in the direction perpendicular to the field. The initial transverse momenta, as well as the instants of ionization, are usually distributed in accord with the static ionization rate [23] with the field strength equal to the instantaneous field at the time of ionization.

In the standard formulation, the trajectory models used in strong-field physics are not able to describe quantum interference effects. Accounting for interference effects in trajectory-based simulations has attracted considerable interest (see, e.g., Refs. [24–27]). The recently developed quantum trajectory Monte Carlo (QTMC) [28] and semiclassical two-step (SCTS) models [29] describe interference structures in photoelectron momentum distributions of the ATI process. These models assign a certain phase to each classical trajectory, and the corresponding contributions of all the trajectories leading to a given asymptotic (final) momentum are added coherently. The QTMC model accounts for the Coulomb potential within the semiclassical perturbation theory. In contrast to this, in the SCTS model the phase associated with every trajectory is obtained using the semiclassical expression for the matrix element of the quantum-mechanical propagator (see Ref. [30]). Therefore, the SCTS model accounts for the binding potential beyond the semiclassical perturbation theory. This explains why for identical initial conditions after the ionization step the SCTS model shows closer agreement with solution of the TDSE than the QTMC model (see Ref. [29]).

The analysis of the photoelectron momentum distributions and energy spectra calculated within both the QTMC and the

---

[*] n79@narod.ru

SCTS models showed that the ATI peaks are qualitatively reproduced by the semiclassical approaches [29]. However, the semiclassical approximation does not quantitatively reproduce the amplitude of the oscillations. The photoelectron spectra calculated within the semiclassical models fall off too rapidly for energies exceeding U_p, where $U_p = F_0^2/4\omega^2$ is the ponderomotive energy, i.e., the cycle-averaged quiver energy of a free electron in an electromagnetic field (atomic units are used throughout the paper unless indicated otherwise). Here, F_0 and ω are the amplitude and the frequency of the field, respectively. This deficiency is closely related to the fact that the initial conditions usually employed in semiclassical models provide too few trajectories with large longitudinal momenta [29].

Recently several approaches to improving the quality of the initial conditions in semiclassical models have been proposed. The simplest method is to distribute the initial conditions for electron trajectories using the SFA formulas (see, e.g., Refs. [31–36]). We note that this method dates back to Refs. [37,38]. In most cases it leads to closer agreement with the TDSE. However, to the best of our knowledge, the validity of the usage of the SFA expressions in trajectory-based simulations has not been systematically analyzed so far. In this paper we consider an alternative approach: the combination of the semiclassical models with direct numerical solution of the TDSE.

A significant step in this direction has been taken with the development of the backpropagation method (see Refs. [39,40]). In this method, the wave packet of the outgoing electron obtained from the TDSE is transformed into classical trajectories. These trajectories are then propagated backwards in time, which makes it possible to retrieve the information about the tunnel exit point and the initial electron velocity. Various approximations to the distributions of the starting points and the initial velocities were analyzed by choosing different criteria to stop the backpropagating trajectories [40,41]. However, the backpropagation method requires the numerical solution of the TDSE up to some point in time after the end of the laser pulse *in the whole space*. This restricts its applicability in the case of computationally difficult strong-field problems.

A promising approach would be a combination of the SCTS model with extended virtual detector theory (EVDT) [42,43]. For the first time the concept of a virtual detector (VD) was proposed in Ref. [44] as a method for calculating momentum distributions from the time-dependent wave function. The EVDT approach combines the VD method with semiclassical simulations. The EVDT employs a network of virtual detectors that encloses an atom interacting with the external laser field. Each detector detects the wave function $\psi(\vec{r},t) = A(\vec{r},t)\exp[i\phi(\vec{r},t)]$ obtained by solving the TDSE and generates a classical trajectory at the same position with the initial momentum $\vec{k}$ determined from the gradient of the phase, $\vec{k}(\vec{r}_d,t) \equiv \nabla\cdot\phi(\vec{r}_d,t) = \vec{j}(\vec{r}_d,t)/|A(\vec{r}_d,t)|^2$. Here $\vec{r}_d$ is the position of a virtual detector and $\vec{j}(\vec{r}_d,t)$ is the probability flux at this position. The latter determines the relative weight of the generated trajectory. The subsequent motion of an electron is found from the solution of Newton's equations. The final photoelectron momentum distribution is obtained by summing over all classical trajectories with their relative weights. It should be stressed that EVDT solves the TDSE only within some restricted region centered at the atom. A network of virtual detectors is placed at the boundary of this region. This reduces the computational load of numerically difficult strong-field problems. Recently the VD approach was used for study of tunneling times [45] and longitudinal momentum distributions [46] in strong-field ionization.

Leaving the combination of the SCTS with the EVDT for future studies, in this paper we formulate an alternative quantum-classical approach: the semiclassical two-step model with quantum input (SCTSQI). To this end, we combine the SCTS model with initial conditions obtained from TDSE solutions using Gabor transforms. For simplicity, we consider ionization of a one-dimensional (1D) atom. The generalization to the real three-dimensional case is straightforward. The benefit of the 1D model, however, is that potential deficiencies of trajectory models are exposed better and, therefore, it makes the comparison with the fully quantum simulations more valuable.

The paper is organized as follows. In Sec. II we sketch our approach to solve the TDSE, we briefly review the SCTS model, and we formulate our SCTSQI approach. In Sec. III we apply our model to the ionization of a 1D model atom and present comparison with the TDSE results. The conclusions and outlook are given in Sec. IV.

II. SEMICLASSICAL TWO-STEP MODEL WITH QUANTUM INPUT

We benchmark our semiclassical model against the results obtained by direct numerical solution of the 1D TDSE and by using the SCTS model. For this reason, before formulating the SCTSQI model and discussing its outcomes, we briefly review the technique used to solve the TDSE and sketch the SCTS model. We define a few-cycle laser pulse linearly polarized along the x axis in terms of a vector potential:

$$\vec{A} = (-1)^{n+1}\frac{F_0}{\omega}\sin^2\left(\frac{\omega t}{2n}\right)\sin(\omega t+\varphi)\vec{e}_x. \tag{1}$$

Here n is the number of the cycles within the pulse, φ is the carrier envelope phase, and $\vec{e}_x$ is a unit vector. The laser pulse is present between $t = 0$ and $t_f = (2\pi/\omega)n$, and its electric field $\vec{F}$ can be obtained from Eq. (1) by $\vec{F} = -\frac{d\vec{A}}{dt}$.

A. Solution of the one-dimensional time-dependent Schrödinger equation

In the velocity gauge, the 1D TDSE for an electron in the laser pulse reads as

$$i\frac{\partial}{\partial t}\Psi(x,t) = \left\{\frac{1}{2}\left(-i\frac{\partial}{\partial x}+A_x(t)\right)^2+V(x)\right\}\Psi(x,t), \tag{2}$$

where $\Psi(x,t)$ is the time-dependent wave function in coordinate space, and a soft-core potential $V(x) = -\frac{1}{\sqrt{x^2+a^2}}$ is used, with $a = 1$ as in Ref. [47].

In the absence of the laser pulse, the 1D system satisfies the time-independent Schrödinger equation:

$$\left\{-\frac{1}{2}\frac{d^2}{dx^2}+V(x)\right\}\Psi(x) = E\Psi(x). \tag{3}$$

We solve Eq. (3) on a grid and approximate the second derivative by the well-known three-point formula. For our simulations we use a box centered at the origin and extending to $\pm x_{\max}$, i.e., $x \in [-x_{\max}, x_{\max}]$. Typically, our grid extends up to $x_{\max} = 500$ a.u. and consists of 8192 points, which corresponds to the grid spacing $dx \approx 0.1221$ a.u. The energy eigenvalues E_n and the corresponding eigenfunctions $\Psi_n(x)$ are found by a diagonalization routine designed for sparse matrices [48]. For the chosen value of a we find the ground-state energy $E_0 = -0.6698$ a.u. This value, as well as the energies of other lowest-energy bound states, coincides with the results of Ref. [47].

We solve Eq. (2) using the split-operator method [49] with the time step $\Delta t = 0.0734$ a.u. Unphysical reflections of the wave function from the grid boundary are prevented by using absorbing boundaries. More specifically, in the region $|x| \geqslant x_b$ we multiply the wave function by a mask

$$M(x) = \cos^{1/6}\left[\frac{\pi(|x| - x_b)}{2(x_{\max} - x_b)}\right]. \tag{4}$$

Here we assume that the internal boundaries of the absorbing regions correspond to $x = \pm x_b$ (we use $x_b = 3x_{\max}/4$). This ensures that the part of the wave function in the mask region is absorbed without an effect on the inner part $|x| < x_b$. We calculate the photoelectron momentum distributions using the mask method (see Ref. [50]).

B. Semiclassical two-step model

In our semiclassical simulations the trajectory $\vec{r}(t)$ and momentum $\vec{p}(t)$ of an electron are calculated treating the electric field of the pulse $\vec{F}(t)$ and the ionic potential $V(\vec{r}, t)$ on equal footing:

$$\frac{d^2\vec{r}}{dt^2} = -\vec{F}(t) - \vec{\nabla}V(\vec{r}, t). \tag{5}$$

In the SCTS model, every trajectory is associated with the phase of the matrix element of the semiclassical propagator [30]. For an arbitrary effective potential $V(\vec{r}, t)$ the SCTS phase reads as

$$\Phi(t_0, \vec{v}_0) = -\vec{v}_0 \cdot \vec{r}(t_0) + I_p t_0 - \int_{t_0}^{\infty} dt \left\{\frac{p^2(t)}{2} + V[\vec{r}(t)] - \vec{r}(t)\cdot\vec{\nabla}V[\vec{r}(t)]\right\}, \tag{6}$$

where t_0 is the ionization time, and $\vec{r}(t_0)$ and $\vec{v}_0$ are the initial electron position and velocity of an electron, respectively.

We solve Newton's equations of motion (5), in order to find the final (asymptotic) momenta of all the trajectories, and bin them in cells in momentum space according to these final momenta. If the quantum interference is taken into account, a large number of classical trajectories is needed in order to achieve convergence of electron momentum distributions. Different approaches of sampling the initial conditions can be used. In one possible approach the initial conditions, i.e., the ionization times t_0^j and transverse initial velocities $\vec{v}_{0,\perp}^j$ ($j = 1, \ldots, n_p$) of the ensemble consisting of n_p trajectories are distributed randomly, or, equivalently, a uniform grid in the $(t_0, \vec{v}_0)$ space is used. The weight of each trajectory is determined by the corresponding tunneling probability. The latter is given by the formula for the static ionization rate [23]:

$$w(t_0, v_{0,\perp}) \sim \exp\left(-\frac{2(2I_p)^{3/2}}{3F(t_0)}\right)\exp\left(-\frac{\kappa v_{0,\perp}^2}{F(t_0)}\right), \tag{7}$$

where $\vec{v}_{0,\perp}$ is the initial electron velocity in the direction perpendicular to the instantaneous laser field $\vec{F}(t_0)$ at the time of ionization. Here it is assumed that the electron emerges at the tunnel exit from the potential barrier formed by the instantaneous field and the ionic potential with zero initial velocity along the laser field: $\vec{v}_{0,||} = 0$. Indeed, in the tunneling picture the electron velocity in the direction of tunneling must be equal to zero at the turning point. However, the tunneling makes no restriction on the perpendicular velocity. This is supported by the tunneling theory (see Ref. [20]). The contributions of the $n_{\vec{k}}$ trajectories that reach the same bin centered at a given final momentum $\vec{k}$ are added coherently. Therefore, the ionization probability is given by

$$R(\vec{k}) = \left|\sum_{j=1}^{n_{\vec{k}}} \sqrt{w\left(t_0^j, \vec{v}_{0,\perp}^j\right)}\exp\left[i\Phi\left(t_0^j, \vec{v}_{0,\perp}^j\right)\right]\right|^2. \tag{8}$$

Alternatively, we can take into account the weight of a given trajectory before the solution of Newton's equations, i.e., already at the sampling stage. To this end, we distribute the sets of initial conditions $(t_0^j, \vec{v}_{0,\perp}^j)$ in accord with the square root of the tunneling probability (see Ref. [29] for details). We refer to this implementation of the SCTS model as the importance sampling implementation. We note that a similar approach is widely used in Monte Carlo integration (see Ref. [51]). If the trajectories are selected by importance sampling, the ionization probability in the SCTS model is calculated as

$$R(\vec{k}) = \left|\sum_{j=1}^{n_{\vec{k}}} \exp\left[i\Phi\left(t_0^j, \vec{v}_0^j\right)\right]\right|^2. \tag{9}$$

For some laser parameters the importance sampling approach can significantly decrease the computational cost of the SCTS model. In the present work we use the important sampling implementation of the SCTS model. However, in our SCTSQI model we employ the first approach with random distribution of the initial conditions (see Sec. II B).

If the potential $V(\vec{r}, t)$ is set to the 1D soft-core potential $V(x) = -1/\sqrt{x^2 + a^2}$, the equation of motion (5) and the expression for the SCTS phase (6) reads as

$$\frac{d^2x}{dt^2} = -F_x(t) - \frac{x}{(x^2 + a^2)^{3/2}}, \tag{10}$$

and, choosing the initial velocity as zero, we have the phase

$$\Phi(t_0, \vec{v}_0) = I_p t_0 - \int_{t_0}^{\infty} dt \left\{\frac{v_x^2(t)}{2} - \frac{x^2}{(x^2 + a^2)^{3/2}} - \frac{1}{\sqrt{x^2 + a^2}}\right\} dt. \tag{11}$$

In the 1D case the ionization rate (7) is replaced by

$$w(t_0) \sim \exp\left(-\frac{2(2|E_0|)^{3/2}}{3F(t_0)}\right), \tag{12}$$

where $E_0 = -0.6698$ a.u. is the ground-state energy in the potential $V(x)$.

We integrate the equation of motion numerically up to $t = t_f$ and find the final electron momentum k_x from its momentum $p_x(t_f)$ and position $x(t_f)$ at the end of the laser pulse. To this end, the energy conservation law can be used. Since an unbound classical electron cannot change the direction of its motion at $t \geqslant t_f$, the sign of the k_x coincides with that of $p_x(t_f)$.

In order to accomplish the formulation of the SCTS model for the 1D case, we need to calculate the postpulse phase, i.e., the contribution to the phase (11) accumulated in the asymptotic interval $[t_f, \infty]$. Indeed the phase of Eq. (11) can be decomposed as

$$\begin{aligned}\Phi(t_0, \vec{v}_0) &= I_p t_0 - \int_{t_0}^{t_f} dt \left\{\frac{v_x^2(t)}{2} - \frac{x^2}{(x^2+a^2)^{3/2}} - \frac{1}{\sqrt{x^2+a^2}}\right\} \\ &\quad + \Phi_f^V,\end{aligned} \tag{13}$$

where the postpulse phase Φ_f^V reads

$$\Phi_f^V(t_f) = -\int_{t_f}^{\infty} \left(E - \frac{x^2(t)}{[x^2(t)+a^2]^{3/2}}\right) dt \tag{14}$$

with total energy E. As in Ref. [29], we separate the phase (14) into parts with time-independent and time-dependent integrand. The first part yields the linearly divergent contribution

$$\lim_{t\to\infty} (t_f - t)E \tag{15}$$

that is to be disregarded, since it results in the zero phase difference for the trajectories leading to the same momentum cell. Therefore, the postpulse phase is determined by the time-dependent contribution

$$\tilde{\Phi}_f^V = \int_{t_f}^{\infty} \frac{x^2(t)}{[x^2(t)+a^2]^{3/2}} dt. \tag{16}$$

Although the integral (16) diverges, we can isolate the divergent part as follows:

$$\begin{aligned}\tilde{\Phi}_f^V &= \int_{t_f}^{\infty} \left[\frac{x^2}{(x^2+a^2)^{3/2}} - \frac{2Et^2}{(2Et^2+a^2)^{3/2}}\right] dt \\ &\quad + \int_{t_f}^{\infty} \frac{2Et^2}{(2Et^2+a^2)^{3/2}} dt.\end{aligned} \tag{17}$$

The divergent contribution, i.e., the second term of Eq. (17), depends only on the electron energy E and parameter a and, therefore, is equal for all the trajectories leading to a given bin on the p_x axis. Since we are interested in the relative phases of the interfering trajectories, this common divergent part can be omitted, and the postpulse phase can be calculated as

$$\overset{\approx}{\Phi}{}_f^V = \int_{t_f}^{\infty} \left[\frac{x^2}{(x^2+a^2)^{3/2}} - \frac{2Et^2}{(2Et^2+a^2)^{3/2}}\right] dt. \tag{18}$$

The integral in Eq. (18) converges and can be easily calculated numerically. It depends on the electron position $x(t_f)$ and velocity $v_x(t_f)$ at the end of the pulse. In practice, we calculate this integral on a grid in the $(x(t_f), v_x(t_f))$ plane and use bilinear interpolation, in order to find its values for $x(t_f)$ and $v_x(t_f)$ that correspond to every electron trajectory.

C. Semiclassical two-step model with quantum input

Combination of the exact solution of the TDSE with a trajectory-based model is not a simple task. In order to calculate a classical trajectory, both the starting point and the initial velocity are needed. However, in accord with Heisenberg's uncertainty principle, there is a fundamental limit to the precision with which canonically conjugate variables such as position and momentum can be known. Information about *both* the position and momentum of a quantum particle can be obtained using a position-momentum quasiprobability distribution, e.g., the Wigner function or Husimi distribution (see, e.g., Ref. [52] for a textbook treatment). Here we employ the Gabor transformation [53], which is widely used for the analysis of the HHG and ATI (see, e.g., Refs. [54–57]). The Gabor transformation of a function $\tilde{\Psi}(x,t)$ near the point x_0 is defined by

$$\begin{aligned}G(x_0, p_x, t) = \frac{1}{\sqrt{2\pi}} \int_{-\infty}^{\infty} \tilde{\Psi}(x', t) \exp\left[-\frac{(x'-x_0)^2}{2\delta_0^2}\right] \\ \times \exp(-ip_x x') dx',\end{aligned} \tag{19}$$

where the exponential factor $\exp\left[-\frac{(x'-x_0)^2}{2\delta_0^2}\right]$ is a window with the width δ_0. The squared modulus of $G(x_0, p_x, t)$ describes the momentum distribution of the electron in the vicinity of $x = x_0$ at time t. In fact, $|G(x_0, p_x, t)|^2$ is nothing but the Husimi distribution [58], which can be obtained by a Gaussian smoothing of the Wigner function. In contrast to the Wigner function, the Husimi distribution is a positive-semidefinite function, which facilitates the interpretation as a quasiprobability distribution. In our SCTSQI model, we solve the TDSE in the length gauge:

$$i\frac{\partial}{\partial t}\Psi(x,t) = \left\{-\frac{1}{2}\frac{\partial^2}{\partial x^2} + V(x) + F_x(t)x\right\}\Psi(x,t). \tag{20}$$

We introduce two additional spatial grids consisting of N points in the absorbing regions of the computational box:

$$x_{0,\pm}^j = \mp(x_b + \Delta x \cdot j), \tag{21}$$

where $\Delta x = (x_{\max} - x_b)/N$ and $j = 0, \ldots, N$. At every step of the time propagation of the TDSE (20) we calculate the Gabor transform (19) of the absorbed part $\tilde{\Psi}(x,t) = [1 - M(x)]\Psi(x,t)$ at the points $x_{0,-}^j$ and $x_{0,+}^j$ [see Fig. 1(a)]. The TDSE is solved in the computational box $x \in [-x_{\max}, x_{\max}]$, whereas the Gabor transforms are calculated only for $x \in [-x_{\max}, x_b]$ and $x \in [x_b, x_{\max}]$. However, in the SCTSQI model the size of the computational box can be chosen much smaller than the one required to obtain accurate electron momentum distributions (see Sec. III). As a result, at every time instant t we know $G(x, p_x, t)$ on the grids in the rectangular domains $D_1 = [-x_{\max}, -x_b] \times [-p_{x,\max}, p_{x,\max}]$ and $D_2 = [x_b, x_{\max}] \times [-p_{x,\max}, p_{x,\max}]$ of the phase space. Here $p_{\max}$ is the maximum momentum, i.e., $p_{\max} = \pi/\Delta x$,

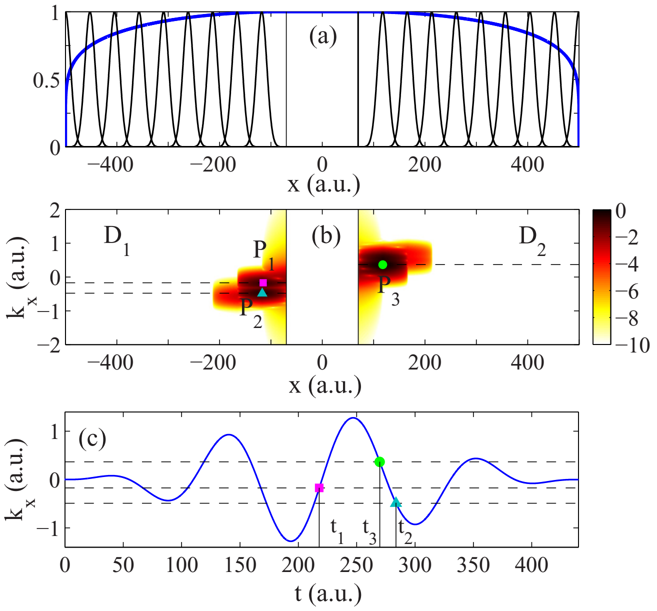

FIG. 1. (a) Scheme illustrating the structure of the computational box in the SCTSQI model. The mask function [Eq. (4)] is shown by the thick blue curve. The vertical lines correspond to the internal boundaries of the mask region. The thin black curves show the windows of the Gabor transform centered at the points $x_{0,\pm}^i$ [Eq. (21)]. (b) The Husimi quasiprobability distribution $|G(x, p_x, 3t_f/2)|^2$ calculated at $t = 3t_f/2$ for the laser pulse defined by Eq. (1) with a duration of $n = 4$ cycles, intensity of 2.0×10^{14} W/cm^2, phase $\varphi = 0$, and a wavelength of 800 nm. The Husimi distribution is calculated in the domains D_1 and D_2 of the phase space (see text). A logarithmic color scale is used. P_1–P_3 represent the three main spots of the Husimi distribution. The maxima of these spots are depicted by a (green) circle, (magenta) square, and (cyan) rectangle, respectively. (c) The final electron momentum $-A_x(t)$ in the potential-free classical model as a function of the time of ionization. The parameters of the laser pulse are the same as in (b). The vicinities of the time instants t_1, t_2, and t_3 make the main contribution to the spots P_1, P_2, and P_3, respectively [see (b)].

if the fast Fourier transform is used to calculate Eq. (19). An example of the corresponding Husimi quasiprobability distribution calculated at $t = 3t_f/2$ is shown in Fig. 1(b). At this time instant the quasiprobability distribution consists of the three main spots P_1, P_2, and P_3, whose maxima are indicated by a (green) circle, (magenta) square, and (cyan) triangle, respectively. These maxima correspond to the electron momenta k_x equal to 0.37, −0.17, and −0.48 a.u., respectively [see Fig. 1(b)]. According to the two-step model, a final electron momentum k_x corresponds to the ionization times t_0 satisfying the equation

$$k_x = -A_x(t_0). \tag{22}$$

Depending on the momentum value, this equation can have several solutions, and therefore, several different ionization times can lead to a given k_x; see Fig. 1(c), which shows the final electron momentum as a function of the ionization time. The analysis of the time evolution of the electron probability density reveals that every spot in Fig. 1(b) is mainly created within a narrow time interval that is close to only one of the solutions of Eq. (22). The solutions of Eq. (22) that make the main contributions to the maxima of P_1, P_2, and P_3 are shown in Fig. 1(c). This fact is easy to understand, if we take into account that Fig. 1(b) is a snapshot of the dynamic quasiprobability distribution in the absorbing mask regions. Indeed, at a given time instant the contributions to the Husimi distribution from the vicinities of other solutions of Eq. (22) are either already absorbed by the mask or have not reached the absorbing regions yet. We note that aside from P_1, P_2, P_3 some other less pronounced spots are also seen in Fig. 1(b). These latter spots correspond to the contributions that by the given time instant are already mostly absorbed. The slight slope of the whole Husimi distribution that is visible in Fig. 1(b) is due to the fact that the contributions corresponding to the high values of $|k_x|$ travel larger distances before being absorbed than the ones with smaller $|k_x|$.

The value of the Gabor transform at an arbitrary point that belongs to the domain D_1 or D_2 can be obtained by a two-dimensional interpolation. We note that the application of the additional grids (21) in combination with the two-dimensional interpolation provides a computationally cheap alternative to the calculation of the Gabor transform at all the points of the main spatial grid that fall within the absorbing regions. The accuracy with which the function $G(t, x, p_x)$ is calculated depends on the number of points, N, in the grids (21) and, therefore, the convergence of the results with respect to this number must be checked.

Let N_T be the number of time steps used to solve the TDSE. At every time point t_0^m $(m = 1, \ldots, N_T)$ used for the time propagation of the TDSE we randomly distribute initial positions x_0^j and momenta $p_{x,0}^j$ $(j = 1, \ldots, n_p)$ of n_p classical trajectories in the domains D_1 and D_2. These trajectories are propagated according to Newton's equation of motion (10). Every trajectory is assigned with the quantum amplitude $G(t_0, x_0^j, p_{x,0}^j)$ and the phase

$$\Phi_0(t_0, x_0^j, p_{x,0}^j) = -\int_{t_0}^{\infty} dt \left\{ \frac{v_x^2(t)}{2} - \frac{x^2}{(x^2+a^2)^{3/2}} - \frac{1}{\sqrt{x^2+a^2}} \right\}. \tag{23}$$

We note that the SCTSQI phase (23) corresponds to the phase of the matrix element of the semiclassical propagator that describes a transition from momentum $p_{x,0}^j$ at $t = t_0$ to momentum $k_x^j = k_x^j(x_0^j, p_{x,0}^j)$ at $t \to \infty$. The ionization probability in the SCTSQI model is given by

$$R(k_x) = \left| \sum_{m=1}^{N_T} \sum_{j=1}^{n_{k_x}} G(t_0^m, x_0^j, p_{x,0}^j) \exp\left[i\Phi_0(t_0^m, x_0^j, p_{x,0}^j) \right] \right|^2, \tag{24}$$

where n_{k_x} is the number of trajectories reaching the same bin centered at k_x [cf. Eq. (8)]. It should be stressed that the Gabor transform $G(t_0^m, x_0^j, p_{x,0}^j)$ is a complex function with both absolute value and phase. In order to ensure that ionized parts of the wave function reach the absorbing regions, we propagate the TDSE up to some time $t = T$, where $T > t_f$. For this reason, in the SCTSQI model we calculate classical trajectories till $t = T$ and replace t_f by T in Eq. (18) for the postpulse phase. In our simulations we have used $T = 4t_f$.

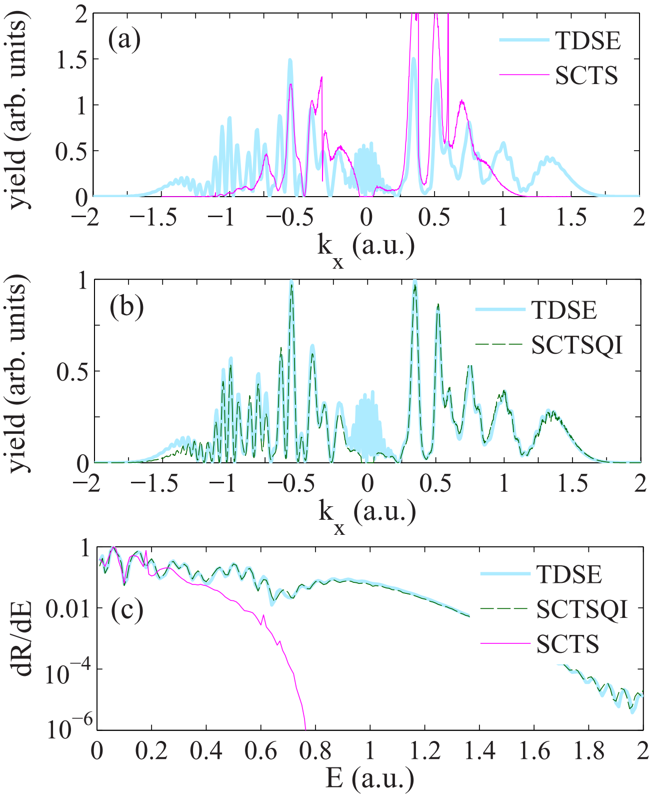

FIG. 2. Comparison of the semiclassical models with the TDSE. The parameters are the same as in Fig. 1(b). (a) The photoelectron momentum distributions for ionization of a one-dimensional model atom obtained from the SCTS model (thin magenta curve) and the solution of the TDSE (thick light blue curve). The distributions are normalized to the total ionization yield. (b) The electron momentum distributions calculated using the present SCTSQI model (dashed dark green curve) and the TDSE (thick light blue curve). The distributions are normalized to the peak values. (c) Electron energy spectra obtained from the TDSE (thick light blue curve), SCTSQI (dashed dark green curve), and the SCTS (thin magenta curve). The spectra are normalized to the peak values.

III. RESULTS AND DISCUSSION

For our numerical examples we use the intensity of 2.01×10^{14} W/cm^2 ($F_0 = 0.0757$ a.u.) and the wavelength 800 nm ($\omega = 0.057$ a.u.). This corresponds to the Keldysh parameter $\gamma = \omega\sqrt{2I_p}/F_0$ (see Ref. [6]) equal to 0.87. For simplicity, we set the absolute phase of the pulse (1) equal to zero: $\varphi = 0$.

We benchmark our SCTSQI approach against the SCTS model and the exact numerical solution of the TDSE. We implement the SCTS by solving Newton's equation of motion using a fourth-order Runge-Kutta method with adaptive step size [51]. In order to fully resolve the rich interference structure, we need to use the a momentum-space bin size of $\Delta k_x = 0.0019$ a.u. For this value of Δk_x the convergence of the interference oscillations is achieved for an ensemble consisting of 1.2×10^7 trajectories. At first, we consider photoelectron momentum distributions. In Fig. 2(a) we compare the SCTS model with the solution of the TDSE. The TDSE photoelectron momentum distribution has a rather complicated structure. This is due to the fact that the laser pulse used in calculations is neither long nor very short. The side maxima at $k_x = -1.35$ a.u. and $k_x = 1.33$ a.u. are created due to the interference of contributions from times near the central maximum and minimum of the vector potential, respectively [see Fig. 1(c)]. The central minimum of the vector potential is also responsible for the formation of the maximum at $k_x = 1.0$ a.u. On the other hand, the ATI peaks in the electron momentum distributions are most pronounced in the range of k_x from -1.0 to -0.25 a.u. The SCTS model predicts a caustic of the momentum distribution around $k_x = 0.38$ a.u. For this reason, we normalize the distributions of Fig. 2(a) to the total ionization yield. Figure 2(a) shows that there is only a qualitative agreement between the SCTS approach and the TDSE result. Indeed, the SCTS model underestimates the width of the momentum distribution.

In Fig. 2(b) we compare the SCTSQI model with the TDSE. In our SCTSQI simulations we have used $N = 50$, $x_{\max} = 500$ a.u., and $x_b = 70$ a.u. We note that in the SCTSQI approach, as well as in the SCTS model, the convergence of the electron momentum distributions must be achieved with respect to both the size of the bin and the number of trajectories. In order to achieve convergence of the momentum distribution, the bin size was chosen to be 1.5×10^{-4} a.u., and $n_p = 10^6$ trajectories were launched at every time step of the TDSE propagation. We note that in the mask method it is difficult to achieve full convergence of the TDSE momentum distribution for small momenta. The distribution in the vicinity of $k_x = 0$ is formed by the slow parts of the electron wave packet. A long propagation time is needed in order to let these parts reach the absorbing mask and, therefore, to obtain converged distribution for small k_x. Thus we do not consider the region of small k_x when comparing the SCTSQI model with the TDSE. It is clearly seen from Fig. 2(b) that for $|k_x| \gtrsim 0.15$ a.u. the SCTSQI model provides *quantitative* agreement with a fully quantum-mechanical result. This applies to both the width of the momentum distribution and the positions of the interference maxima (minima). The small remaining discrepancy in the heights of some of the interference maxima is caused by the fact that, similar to the SCTS, the SCTSQI model does not account for the preexponential factor of the semiclassical matrix element [30].

In Fig. 2(c) we present the photoelectron energy spectra obtained from the SCTS, the solution of the TDSE, and the present SCTSQI model. It is seen that the SCTSQI and the TDSE spectra are almost identical, while the spectrum predicted by the SCTS model falls off too rapidly with the increase of the electron energy. This is a direct consequence of the fact that the SCTS model underestimates the width of the electron momentum distribution [see Fig. 2(a)].

In order to further test the SCTSQI model, we calculate the electron momentum distributions for different positions of the mask x_b and fixed $x_{\max}$ of the computational box [see Fig. 3(a)]. The distributions corresponding to different values of x_b are in good quantitative agreement with each other. The same is also true for momentum distributions obtained for fixed x_b and different values of $x_{\max}$ [see Fig. 3(b)]. Here, we have used the two values $x_{\max} = 500$ a.u. and $x_{\max} = 200$ a.u. It should be stressed that it is impossible to obtain accurate electron momentum distributions for the small value $x_{\max} = 200$ a.u. using the mask method. We also note that for the 1D

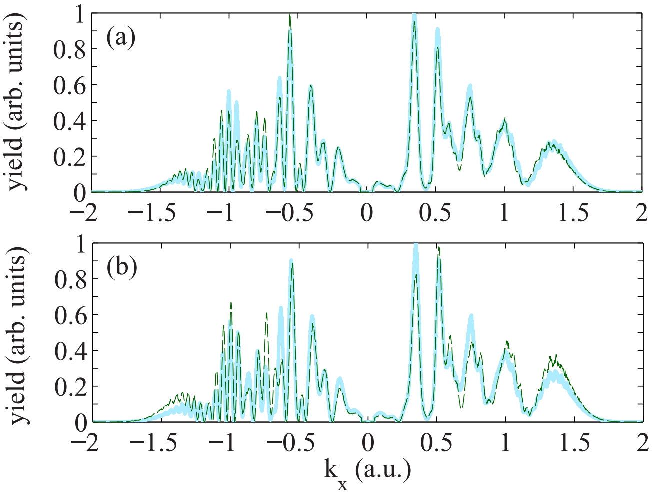

FIG. 3. The outcomes of the SCTSQI model for different internal boundaries of the absorbing mask and lengths of the computational box. The distributions are normalized to the peak values. (a) The one-dimensional momentum distributions calculated within the SCTSQI model for the absorbing mask beginning at $x_b = 50$ a.u. (thick light blue curve) and $x_b = 100$ a.u. (dashed dark green curve). The parameters are the same as in Fig. 1(b), and the size of the computational box is $x_{\max} = 500$ a.u. (b) The one-dimensional momentum distributions obtained from the SCTSQI model for $x_{\max} = 500$ a.u. (thick light blue curve) and $x_{\max} = 200$ a.u. (dashed dark green curve). The parameters are the same as in Fig. 1(b). The absorbing mask begins at $x_b = 50$ a.u.

soft-core Coulomb potential used in this work, the smallest allowed x_b should exceed 30–40 a.u., to be outside of the region where the bound-state wave function is localized. Indeed, due to the large number of time steps, even the absorption of a small fraction of the bound-state wave function at each step will result in a severe distortion of the final momentum distribution.

Finally, we check how important is the phase of the factor $G(x, p_x, t)$ in Eq. (24). To this end, in Fig. 4 we compare the photoelectron momentum distribution calculated using the formula

$$R(k_x) = \left| \sum_{m=1}^{N_T} \sum_{j=1}^{n_{k_x}} \left| G\left(t_0^m, x_0^j, p_{x,0}^j\right) \right| \exp\left[i\Phi_0\left(t_0^m, x_0^j, p_{x,0}^j\right)\right] \right|^2, \tag{25}$$

instead of Eq. (24). We find that neglecting the phase of the Gabor transform is severe: The SCTSQI distribution cannot even be qualitatively reproduced when using Eq. (25). This result could be expected. Indeed, the factor $G(x, p_x, t)$ contains all the information about the quantum dynamics of the absorbed part of the wave packet *prior* to its conversion to the ensemble of classical trajectories. In a sense the $I_p t_0$ term in the SCTS phase [see Eq. (11)] plays the role of the phase $G(t, x, p_x)$ of the Gabor transform in Eq. (24).

We also study the role of the maximal allowed initial momentum $p_{x,\max}$. To this end, we perform the SCTSQI simulations for $p_{x,\max} = 1.0$ a.u. and $p_{x,\max} = 0.5$ a.u. [see Fig. 4(b)]. This should be compared with $p_{x,\max} = 2.0$ a.u. used above. It is seen that the width of the photoelectron momentum distribution decreases with decreasing $p_{x,\max}$. However, reducing the D_1 and D_2 domains in the p_x direction does not make the SCTSQI approach coincide with the SCTS model [see Fig. 4(b)]. This result could be expected. Indeed, electron trajectories start at different points in the SCTSQI and the SCTS models. The SCTS model relies on an expression for the tunnel exit point, whereas in the SCTSQI model every trajectory can start at any point of space in the absorbing regions. Figures 4(a) and 4(b) indicate that the phase of the Gabor transform and the maximal allowed initial momentum are equally important for reproducing of the TDSE result.

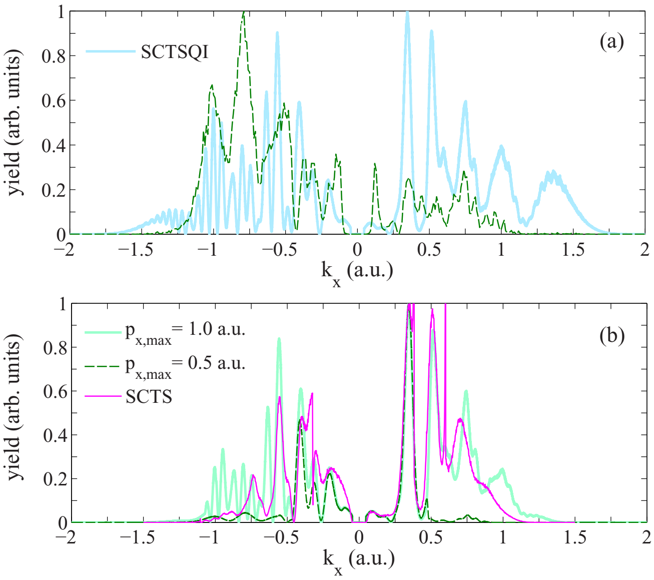

FIG. 4. (a) The photoelectron momentum distributions obtained from the SCTSQI model (thick light blue curve) and using Eq. (25), i.e., neglecting the phase of the Gabor transform (dashed dark green curve). The parameters are the same as in Figs. 1(b), 2, and 3. The size of the computational box is $x_{\max} = 500$ a.u., and the absorbing mask begins at $x_b = 50$ a.u. The distributions are normalized to the peak values. (b) The one-dimensional momentum distributions obtained from the SCTSQI model for $p_{x,\max} = 1.0$ a.u. (thick light blue curve) and $p_{x,\max} = 0.5$ a.u. (dashed dark green curve). The thin magenta curve shows the result of the SCTS model. The parameters are the same as in Figs. 1(b), 2, and 3. The distributions calculated within the SCTSQI model are normalized to the peak values, whereas the one obtained from the SCTS model is normalized to the value at $k_x = 0.35$ a.u. for visual convenience.

As other trajectory-based approaches, our SCTSQI model can help to illustrate the physical mechanisms underlying the strong-field process under investigation in terms of classical trajectories. In order to illustrate this point, we analyze the formation of the maximum of electron momentum distribution at $k_x = 0.35$ a.u. [see Figs. 2(a) and 2(b)]. We note that the SCTS model reproduces the position and the width of this peak, but not its relative height. First, we identify the trajectories leading to this final momentum in accord with the SCTSQI model. The analysis reveals that there are four main groups of these trajectories. In Fig. 5 we show one typical trajectory from each group (thick curves). The SCTS model also predicts four different groups of trajectories leading to

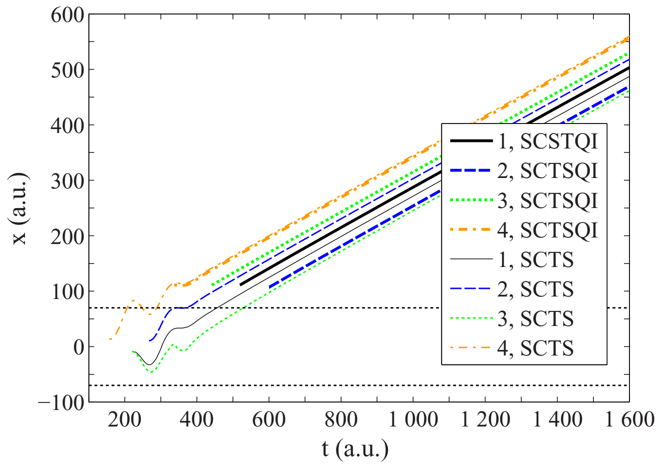

FIG. 5. Four characteristic electron trajectories leading from the SCTSQI and the SCTS models to the same final momentum $k_x = 0.35$ a.u. The parameters are the same as in Figs. 1(b), 2, and 3. The thick curves show the trajectories predicted by the SCTSQI model. The thin curves correspond to the trajectories obtained within the SCTS model. The horizontal dotted lines depict the boundaries of the absorbing regions.

$k_x = 0.35$ a.u. The corresponding characteristic trajectories are shown in Fig. 5 by thin curves. We note that the SCTS trajectories start closer to the origin and at earlier times than the trajectories in the SCTSQI model. This is easy to understand, since classical trajectories in the SCTSQI model can start only within the absorbing regions, i.e., for $|x| > x_b$, and it takes some time for the ionized part of the electron wave function to reach these regions. It is seen from Fig. 5 that the characteristic trajectories are different in the two models. In the SCTSQI model the initial conditions for the electron trajectories are determined from the solution of the TDSE. Therefore, we can expect that the SCTSQI model provides a more accurate trajectory-based picture of the formation of the electron momentum distribution than the SCTS model. This advantage of the SCTSQI approach should be used in the future for the analysis of more complex strong-field processes.

We believe that the SCTSQI model can also be applied to rescattering-induced processes, i.e., high-order ATI, HHG, and NSDI. Knowing the Gabor transform and the phases of the classical trajectories, we can reconstruct the electron wave function in both coordinate and momentum representation not only at $t \to \infty$ [see Eq. (24)], but at any time t. This wave function can be used for calculation of the elastic scattering of the electron wave packet, which is formed in an ionization process, on the parent ion, i.e., for description of the high-order ATI. Alternatively, it can be used, after adding the bound-state wave function, to calculate the expectation values of the electron dipole moment, velocity, or acceleration and, therefore, it allows us to obtain the HHG spectra. The application of the SCTSQI model to the NSDI process is more involved, since it requires solution of the two-electron TDSE, although in a smaller area of space compared to the fully quantum approach.

Finally, we discuss the computational performance of the SCTSQI approach. It should be noted that in the 1D case the SCTSQI model is computationally more expensive than the numerical solution of the TDSE. This is easy to understand taking into account that at every time step the SCTSQI model requires calculation of a number of Gabor transforms, as well as the time propagation of a large ensemble of classical trajectories. The latter is the performance bottleneck of the method. In the present 1D implementation of the SCTSQI model we use about 2×10^{10} trajectories in total. This estimate is done based on the number of time steps needed for the propagation of the TDSE and amount of trajectories launched at every time step.

Nevertheless, we can expect that for the two-dimensional (2D) and three-dimensional (3D) cases the computational complexity of the SCTSQI model will not be higher than the one of the numerical solution of the TDSE. Indeed, for higher dimensionalities the computational costs of the solution of the TDSE increase dramatically. We note that in our SCTS model these costs can be substantially reduced using a smaller computational box compared to the one that is typically needed for solution of the TDSE. On the other hand, computational loads required for integration of Newton's equation of motion are comparable in the 1D, 2D, and 3D cases. Therefore, for higher dimensionalities numerical costs needed for calculation of the ensemble of classical trajectories become less important. In addition to this, an approach similar to the one used in the 1D case can be applied for calculation of the Gabor transform for higher dimensionalities: The Gabor transform can be first calculated on a sparse grid, and its value at any intermediate point is found using linear interpolation. We also note that the number of trajectories required for convergence of electron momentum distributions depends on the size of the bin, observable of interest, and the method used for sampling of initial conditions.

IV. CONCLUSIONS AND OUTLOOK

In conclusion, we have developed a trajectory-based approach to strong-field ionization: the semiclassical two-step model with quantum input. In the SCTSQI model every trajectory is associated with the SCTS phase and, therefore, the SCTSQI model allows us to describe quantum interference and account for the ionic potential beyond the semiclassical perturbation theory. Furthermore, the SCTSQI model corrects the inaccuracies of the SCTS model in treating the tunneling step. This has been achieved by the numerical solution of the TDSE with absorbing boundary conditions in a restricted area of space, applying the Gabor transform to the part of the wave function that is absorbed at each time step, and transforming this absorbed part into classical trajectories. The Gabor transform determines quantum amplitudes assigned to trajectories of the ensemble. Therefore, in the SCTSQI model the initial conditions of classical trajectories are governed by the exact quantum dynamics rather than by the quasistatic or SFA-based expressions as in other semiclassical approaches.

We have tested our SCTSQI model by comparing its predictions with the numerical solution of the 1D TDSE. We have shown that the SCTSQI model yields quantitative agreement with the fully quantum results. This is true not only for the widths of the electron momentum distributions, but also for the positions of the interference maxima and minima. The model can be straightforwardly extended to the three-dimensional case. Most importantly, the SCTSQI model circumvents the nontrivial problem of choosing the initial conditions for classical trajectories. This makes the SCTSQI model extremely useful for study of strong-field ionization of molecules.

ACKNOWLEDGMENTS

We are grateful to Prof. Lars Bojer Madsen (Aarhus University), as well as to Nicolas Eicke and Simon Brennecke (Leibniz Universität Hannover) for stimulating discussions. This work was supported by the Deutsche Forschungsgemeinschaft (Grant No. SH 1145/1-1).

---

[1] N. B. Delone and V. P. Krainov, *Multiphoton Processes in Atoms* (Springer, Berlin, 2000).

[2] W. Becker, F. Grasbon, R. Kopold, D. B. Milošević, G. G. Paulus, and H. Walther, Above-threshold ionization: From classical features to quantum effects, Adv. At. Mol. Opt. Phys. **48**, 35 (2002).

[3] D. B. Milošević and F. Ehlotzky, Scattering and reaction processes in powerful laser fields, Adv. At. Mol. Opt. Phys. **49**, 373 (2003).

[4] A. Becker and F. H. M. Faisal, Intense field many-body S-matrix theory, J. Phys. B **38**, R1 (2005).

[5] C. Faria and X. Liu, Electron-electron correlation in strong laser fields, J. Mod. Opt. **58**, 1076 (2011).

[6] L. V. Keldysh, Ionization in the field of a strong electromagnetic wave, Zh. Eksp. Teor. Fiz. **47**, 1945 (1964) [Sov. Phys. JETP **20**, 1307 (1965)].

[7] F. H. M. Faisal, Multiple absorption of laser photons by atoms, J. Phys. B **6**, L89 (1973).

[8] H. R. Reiss, Effect of an intense electromagnetic field on a weakly bounded system, Phys. Rev. A **22**, 1786 (1980).

[9] H. G. Muller, An efficient propagation scheme for the time-dependent Schrödinger equation in the velocity gauge, Laser Phys. **9**, 138 (1999).

[10] D. Bauer and P. Koval, QPROP: A Schrödinger-solver for intense laser-atom interaction, Comput. Phys. Commun. **174**, 396 (2006).

[11] L. B. Madsen, L. A. A. Nikolopoulos, T. K. Kjeldsen, and J. Fernández, Extracting continuum information from $\Psi(t)$ in time-dependent wave-packet calculations, Phys. Rev. A **76**, 063407 (2007).

[12] A. N. Grum-Grzhimailo, B. Abeln, K. Bartschat, D. Weflen, and T. Urness, Ionization of atomic hydrogen in strong infrared laser fields, Phys. Rev. A **81**, 043408 (2010).

[13] S. Patchkovskii and H. G. Muller, Simple, accurate, and efficient implementation of 1-electron atomic time-dependent Schrödinger equation in spherical coordinates, Comput. Phys. Commun. **199**, 153 (2016).

[14] X. M. Tong, A three-dimensional time-dependent Schrödinger equation solver: An application to hydrogen atoms in an elliptical laser field, J. Phys. B **50**, 144004 (2017).

[15] H. B. van Linden van den Heuvell and H. G. Muller, in *Multiphoton processes*, edited by S. J. Smith and P. L. Knight (Cambridge University Press, Cambridge, UK, 1988).

[16] T. F. Gallagher, Above-Threshold Ionization in Low-Frequency Limit, Phys. Rev. Lett. **61**, 2304 (1988).

[17] P. B. Corkum, N. H. Burnett, and F. Brunel, Above-Threshold Ionization in the Long-Wavelength Limit, Phys. Rev. Lett. **62**, 1259 (1989).

[18] K. C. Kulander, K. J. Schafer, and J. L. Krause, in *Super-Intense Laser-Atom Physics*, edited by B. Pireaux, A. L'Hullier, and K. Rzazewski (Plenum, New York, 1993).

[19] P. B. Corkum, Plasma Perspective on Strong-Field Multiphoton Ionization, Phys. Rev. Lett. **71**, 1994 (1993).

[20] L. D. Landau and E. M. Lifshitz, *Quantum Mechanics Non-relativistic Theory*, 2nd ed. (Pergamon, Oxford, 1965).

[21] A. M. Perelomov, V. S. Popov, and M. V. Terent'ev, Ionization of atoms in an alternating electric field, Zh. Eksp. Teor. Fiz. **50**, 1393 (1966) [Sov. Phys. JETP **23**, 924 (1966)].

[22] M. V. Ammosov, N. B. Delone, and V. P. Krainov, Tunnel ionization of complex atoms and of atomic ions in an alternating electromagnetic field, Zh. Eksp. Teor. Fiz. **91**, 2008 (1986) [Sov. Phys. JETP **64**, 1191 (1986)].

[23] N. B. Delone and V. P. Krainov, Energy and angular electron spectra for the tunnel ionization of atoms by strong low-frequency radiation, J. Opt. Soc. Am. B **8**, 1207 (1991).

[24] G. van de Sand and J.-M. Rost, Semiclassical description of multiphoton processes, Phys. Rev. A **62**, 053403 (2000).

[25] M. Spanner, Strong-Field Tunnel Ionization by Real-Valued Classical Trajectories, Phys. Rev. Lett. **90**, 233005 (2003).

[26] C. Zagoya, C.-M. Goletz, F. Grossmann, and J.-M. Rost, Dominant-interaction Hamiltonians for high-order harmonic generation in laser-assisted collisions, Phys. Rev. A **85**, 041401(R) (2012).

[27] C. Zagoya, J. Wu, M. Ronto, D. V. Shalashilin, and C. Faria, Quantum and semiclassical phase-space dynamics of a wave packet in strong fields using initial-value representations, New J. Phys. **16**, 103040 (2014).

[28] M. Li, J.-W. Geng, H. Liu, Y. Deng, C. Wu, L.-Y. Peng, Q. Gong, and Y. Liu, Classical-Quantum Correspondence for Above-Threshold Ionization, Phys. Rev. Lett. **112**, 113002 (2014).

[29] N. I. Shvetsov-Shilovski, M. Lein, L. B. Madsen, E. Räsänen, C. Lemell, J. Burgdörfer, D. G. Arbó, and K. Tőkési, Semiclassical two-step model for strong-field ionization, Phys. Rev. A **94**, 013415 (2016).

[30] W. H. Miller, Classical-limit quantum mechanics and the theory of molecular collisions, Adv. Chem. Phys. **25**, 69 (1974).

[31] T.-M. Yan, S. V. Popruzhenko, M. J. J. Vrakking, and D. Bauer, Low-Energy Structures in Strong-Field Ionization Revealed by Quantum Orbits, Phys. Rev. Lett. **105**, 253002 (2010).

[32] S. V. Popruzhenko and D. Bauer, Strong-field approximation for systems with Coulomb interaction, J. Mod. Opt. **55**, 2573 (2008).

[33] R. Boge, C. Cirelli, A. S. Landsman, S. Heuser, A. Ludwig, J. Maurer, M. Weger, L. Gallmann, and U. Keller, Probing Nonadiabatic Effects in Strong-Field Tunnel Ionization, Phys. Rev. Lett. **111**, 103003 (2013).

[34] C. Hofmann, A. S. Landsman, A. Zielinski, C. Cirelli, T. Zimmermann, A. Scrinzi, and U. Keller, Interpreting electron-momentum distributions and nonadiabaticity in strong-field ionization, Phys. Rev. A **90**, 043406 (2014).

[35] J.-W. Geng, L. Qin, M. Li, W.-H. Xiong, Y. Liu, Q. Gong, and L.-Y. Peng, Nonadiabatic tunneling ionization of atoms in elliptically polarized laser fields, J. Phys. B **47**, 204027 (2014).

[36] M. Li, J.-W. Geng, M. Han, M.-M. Liu, L.-Y. Peng, Q. Gong, and Y. Liu, Subcycle nonadiabatic strong-field tunneling ionization, Phys. Rev. A **93**, 013402 (2016).

[37] G. L. Yudin and M. Yu. Ivanov, Nonadiabatic tunnel ionization: Looking inside a laser cycle, Phys. Rev. A **64**, 013409 (2001).

[38] D. I. Bondar, Instantaneous multiphoton ionization rate and initial distribution of electron momentum, Phys. Rev. A **78**, 015405 (2008).

[39] H. Ni, U. Saalmann, and J.-M. Rost, Tunneling Ionization Time Resolved by Backpropagation, Phys. Rev. Lett. **117**, 023002 (2016).

[40] H. Ni, U. Saalmann, and J.-M. Rost, Tunneling exit characteristics from classical backpropagation of an ionized electron wave packet, Phys. Rev. A **97**, 013426 (2018).

[41] H. Ni, N. Eicke, C. Ruiz, J. Cai, F. Oppermann, N. I. Shvetsov-Shilovski, and L. W. Pi, Tunneling criteria and a nonadiabatic term for strong-field ionization, Phys. Rev. A **98**, 013411 (2018).

[42] X. Wang, J. Tian, and J. H. Eberly, Extended Virtual Detector Theory for Strong-Field Atomic Ionization, Phys. Rev. Lett. **110**, 243001 (2013).

[43] X. Wang, J. Tian, and J. H. Eberly, Virtual detector theory for strong-field atomic ionization, J. Phys. B **51**, 084002 (2018).

[44] B. Feuerstein and U. Thumm, On the computation of momentum distributions within wavepacket propagation calculations, J. Phys. B **36**, 707 (2003).

[45] N. Teeny, C. H. Keitel, and H. Bauke, Virtual-detector approach to tunnel ionization and tunneling times, Phys. Rev. A **94**, 022104 (2016).

[46] J. Tian, X. Wang, and J. H. Eberly, Numerical Detector Theory for the Longitudinal Momentum Distribution of the Electron in Strong Field Ionization, Phys. Rev. Lett. **118**, 213201 (2017).

[47] J. Javanainen, J. H. Eberly, and Q. Su, Numerical simulations of multiphoton ionization and above-threshold electron spectra, Phys. Rev. A **38**, 3430 (1988).

[48] E. Anderson, Z. Bai, C. Bischof, S. Blackford, J. Demmel, J. Dongarra, J. Du. Craz, A. Greenbaum, S. Hammarling, A. McKenney, and D. Sorensen, *LAPACK User's Guide*, 3rd ed. (Society for Industrial and Applied Mathematics, Philadelphia, 1999).

[49] M. D. Feit, J. A. Fleck, and A. Steiger, Solution of the Schrödinger equation by a spectral method, J. Comput. Phys. **47**, 412 (1982).

[50] X. M. Tong, K. Hino, and N. Toshima, Phase-dependent atomic ionization in few-cycle intense laser pulse, Phys. Rev. A **74**, 031405(R) (2006).

[51] W. H. Press, S. A. Teukolsky, W. T. Vetterling, and B. P. Flannery, *Numerical Recipes in Fortran 77: The Art of Scientific Computing*, 2nd ed. (Cambridge University Press, Cambridge, UK, 1992).

[52] L. E. Ballentine, *Quantum Mechanics: A Modern Development* (World Scientific, Singapore, 1998).

[53] D. Gabor, Theory of communication, J. Inst. Electr. Eng. **93**, 429 (1946).

[54] C. C. Chirilă, I. Dreissigacker, E. V. van der Zwan, and M. Lein, Emission times in high-order harmonic generation, Phys. Rev. A **81**, 033412 (2010).

[55] K.-J. Yuan and A. D. Bandrauk, Circularly polarized attosecond pulses from molecular high-order harmonic generation by ultrashort intense bichromatic circularly and linearly polarized laser pulses, J. Phys. B **45**, 074001 (2012).

[56] J. Wu, B. B. Augstein, and C. Figueira de Morisson Faria, Local dynamics in high-order-harmonic generation using Bohmian trajectories, Phys. Rev. A **88**, 023415 (2013).

[57] X. F. Shu, S. B. Liu, and H. Y. Song, Phase-space analysis for ionization processes in the laser-atom interaction using Gabor transformation, Mod. Phys. Lett. B **30**, 1650147 (2016).

[58] K. Husimi, Some formal properties of the density matrix, Proc. Phys. Math. Soc. Jpn. **22**, 264 (1940).